Improved Tropical-Cyclone Flight-Level Wind Estimates Using Routine Infrared Satellite Reconnaissance

JOHN A. KNAFF

NOAA/Center for Satellite Applications and Research, Fort Collins, Colorado

SCOTT P. LONGMORE AND ROBERT T. DEMARIA

Cooperative Institute for Research in the Atmosphere, Colorado State University, Fort Collins, Colorado

DEBRA A. MOLENAR

NOAA/Center for Satellite Applications and Research, Fort Collins, Colorado

(Manuscript received 9 May 2014, in final form 20 October 2014)

ABSTRACT

A new and improved method for estimating tropical-cyclone (TC) flight-level winds using globally and routinely available TC information and infrared (IR) satellite imagery is presented. The developmental dataset is composed of aircraft reconnaissance (1995–2012) that has been analyzed to a 1 km × 10° polar grid that extends outward 165 km from the TC center. The additional use of an azimuthally average tangential wind at 500 km, based on global model analyses, allows the estimation of winds at larger radii. Analyses are rotated to a direction-relative framework, normalized by dividing the wind field by the observed maximum, and then decomposed into azimuthal wavenumbers in terms of amplitudes and phases. Using a single-field principal component method, the amplitudes and phases of the wind field are then statistically related to principal components of motion-relative IR images and factors related to the climatological radius of maximum winds. The IR principal components allow the wind field to be related to the radial and azimuthal variability of the wind field. Results show that this method, when provided with the storm location, the estimated TC intensity, the TC motion vector, and a single IR image, is able to estimate the azimuthal wavenumber 0 and 1 components of the wind field. The resulting wind field reconstruction significantly improves on the method currently used for satellite-based operational TC wind field estimates. This application has several potential uses that are discussed within.

1. Introduction

The estimation of surface winds associated with tropical cyclones (TCs) is important to a variety of public, private, and governmental stakeholders and applications. However, the surface wind field of TCs is rarely, if ever, instantaneously measured with sufficient resolution to provide enough detail for most users and applications. The best depictions of the TC wind field come from storm-centric temporal composite analyses that make use of aircraft-reconnaissance-based (and other) observations over a relatively short time period (e.g., Powell et al. 2009). Fortunately, many of the high temporal resolution (1 and 10 Hz) digital records of flight-level wind vectors and more recently surface wind speed estimates from the Stepped Frequency Microwave Radiometer (SFMR; Uhlhorn et al. 2007) have been archived and exist in sufficient quantities that analyses of flight-level wind fields can be created for a variety of TC cases. Several studies have also provided guidance on how flight-level wind speeds are related to surface wind speeds (e.g., Powell and Black 1990; Franklin et al. 2003; Powell et al. 2009) and what the surface wind inflow angles are as a function of azimuth and radius based on global positioning system dropwindsonde and SFMR data (Zhang and Uhlhorn 2012). Collectively, these data and techniques allow for the

Corresponding author address: John Knaff, NOAA/NESDIS/CIRA, Campus Delivery 1375, Colorado State University, Fort Collins, CO 80523-1375.
E-mail: john.knaff@noaa.gov

DOI: 10.1175/JAMC-D-14-0112.1

estimation of the flight-level wind fields associated with a large sample of TCs.

Geostationary satellites have also provided over 30 yr of routine infrared (IR) window (~11 μm) observations of TCs in the Atlantic and eastern North Pacific Oceans, where most of the digital aircraft reconnaissance data are available. The coincidence of both the IR and aircraft reconnaissance data has already led to methods for estimating the azimuthally averaged flight-level wind profiles and other aspects of TC structure from the azimuthally averaged IR brightness temperature profiles [e.g., Mueller et al. (2006, hereinafter M06); Kossin et al. (2007, hereinafter K07)]. Using simple assumptions of wind asymmetries as a function of motion, both the M06 and K07 methods produce estimates of two-dimensional flight-level winds. From those flight-level wind estimates, flight-level to surface wind reductions can be applied and the surface wind field can be estimated. Both methods provide IR-based proxies to flight-level winds within 200 km of the TC center. These methods can estimate the high wind speed conditions near the TC center that often cannot be accurately estimated from other satellite platforms or methods, as discussed in Knaff et al. (2011). Thus, these IR-based flight-level wind estimate methods, at the time, represented a new satellite data capability. For instance, modified M06-based wind estimates are used to generate the National Environmental Satellite, Data, and Information Service's (NESDIS) Multiplatform Tropical Cyclone Surface Wind Analysis (MTCSWA; Knaff et al. 2011), which provides operational 6-hourly surface wind field estimates for all active global TCs.

While these methods represented a unique observational capability, they estimate the two-dimensional wind field in a rather crude manner. The only azimuthal asymmetries in those wind fields were due to motion and those asymmetries were not a function of radius. The accuracy and minimum size of the radius of maximum wind (RMW) were also hampered by the radial resolution (4 km) and smoothing (half-power wavelengths of 90 km) used to analyze the flight-level winds used in both M06 and K07, as described in M06. In this paper, we look to improve upon these two methods and create a superior depiction of the flight-level field by 1) using several more years of aircraft reconnaissance data; 2) using a higher-resolution wind analysis system to create the developmental wind fields, one that can better depict the radial and azimuthal variations of the winds; and 3) statistically relating two-dimensional IR information to the amplitude and phase of wavenumbers 0, 1, and 2 of the TC wind field on a TC-motion relative polar analysis grid to better represent TC wind field asymmetries.

2. Data and methodology

With the aforementioned goal in mind, the description of the development of an algorithm that estimates flight-level winds in TCs by interrelating two-dimensional features in digital IR imagery to a two-dimensional representation of observed flight-level TC winds is now described.

There are several key pieces of information used to develop such an algorithm, including flight-level TC wind analyses, relationships between storm properties and the RMW, and spatial information from IR satellite imagery. To interrelate such information, a single-field principal component analysis (SFPCA; Bretherton et al. 1992) methodology is used. However, before SFPCA is attempted, the aircraft reconnaissance data and IR data need to be prepared and climatological RMW relationships need to be reviewed.

The TC wind fields are provided by an analysis that makes use of temporally composited flight-level winds (along with SFMR winds when available) following the TC during the compositing interval. SFMR wind speed observations provide additional and independent information about the wind field. This study uses a combination of 1- and 10-Hz aircraft reconnaissance data from two sources, the NOAA research and U.S. Air Force aircraft, from 1995 through 2012, which are available from the NOAA/Hurricane Research Division. These high-temporal-resolution data are tracked following the storm motion and a classical time-to-space compositing technique to convert observations collected over a multiple-hour time "window" to a "range and bearing" location relative to the storm center at the 6-hourly synoptic times starting at 0000 UTC. For this study, the compositing is done over a 9-h window starting 6 h before and extending 3 h following the analysis/synoptic time.

To more accurately composite flight-level observations, center locations or "fix" locations from the operational observation platforms, available in the Automated Tropical Cyclone Forecast (ATCF; Sampson and Schrader 2000) databases, are used to supplement the smoothed depiction of TC location information provided by the best track, also from ATCF. A tensioned cubic spline is used to obtain estimates of the TC positions following the combination of best track and fix positions as a function of time. Incorporating these additional location points from both aircraft reconnaissance and coastal radar installations allows the aircraft data to be more accurately composited with respect to the TC center.

Flight-level-to-surface reduction factors at multiple vertical levels create a basis function to account for

TABLE 1. Description of the maximum flight-level-to-surface wind reduction factors used in this study as a function of storm region and pressure layer.

Pressure layer (PL; hPa)	Eyewall	Outer	Far field
$800 < PL \leq 600$	0.88	0.83	0.75
$900 < PL \leq 800$	0.78	0.78	0.75
$900 < PL \leq 990$	0.73	0.73	0.75
$PL \geq 990$	0.77	0.77	0.76

observations being made at multiple vertical levels. For this study, maximum flight-level-to-surface reduction factors are chosen for the eyewall, outer, and far-field regions at four pressure layers, as recommended by personnel at the National Hurricane Center (NHC) and based on Franklin et al. (2003) (Table 1). These reduction factors also assume that the winds are observed in a convectively active environment. For this study, the eyewall region is considered to be located within 2 times the azimuthally averaged RMW or a maximum of 37 km (20 n mi, 1 n mi = 1.85 km), whichever is smaller. The outer region is the region located beyond the eye region and its outermost extent is 4 times the radius of maximum wind or 148 km, whichever is smaller. This outer region typically captures the inner rainbands (see Rogers et al. 2012). The far field is considered to be all radii beyond twice the outer region. Reduction factors for locations between regions are estimated via linear interpolation.

Following the findings of Franklin et al. (2003), asymmetries to the reduction factors are applied. The asymmetries consist of a 4% variation of the eyewall region reduction factors and a 17% variation of the outer and far-field reduction factors with the maximum being on the left of the TC motion. SFMR flight-level-equivalent winds are estimated by dividing the wind speed by the appropriate flight-level-to-surface wind reduction factor. Similarly, observation at other vertical levels can be adjusted to a common level for analysis.

The analysis of aircraft reconnaissance data follows the variational data-fitting method on a polar grid described in Knaff et al. (2011), which allows for the combined treatment of scalar and vector wind quantities. For these analyses, only observations taken at pressures higher than 600 hPa are used. These observations are adjusted to a common level using the flight-level-to-surface reduction factors as a basis. The analyses are performed at a common 700-hPa level on a polar grid with a resolution of 10° azimuthally by 1 km radially, out to a radius of 165 km from the center. Performing the analysis at 700 hPa, or above the boundary layer, minimizes variations of surface roughness, when composited data are relocated over land. To fit data to an analysis, two additional parameters are set, namely data weights and filter weights.

Data weights are used to provide the relative weights of the data types. Different data weights are prescribed to flight-level wind vectors and SFMR wind speeds based on the corresponding flight-level wind speed, as shown in Table 2. The data weights used here were recommended by personnel at the NHC to preferentially weight SFMR surface wind speeds when flight-level wind speeds exceed hurricane strength (≥64 kt, 1 kt = 0.51 m s^{-1}; C. Landsea 2013, personal communication) and are based on results from Klotz and Uhlhorn (2010). This implies that SFMR provides more information in hurricane-force wind conditions, where flight-level-to-surface reduction factors have a greater influence on the analysis.

This analysis method also uses filter weights for the radial and azimuthal directions. The filter weights, in this case, were chosen so that the half-power wavelengths were 4 km and 70° in the radial and azimuthal directions, respectively. These filter weight choices result in relatively little smoothing being applied in the radial direction and enough smoothing in the azimuthal direction to make optimal use of the incomplete spatial coverage of aircraft data (e.g., an alpha or figure-four pattern).

For each composited flight-level dataset, the analysis scheme was run three times. Initially the analysis uses winds that are adjusted to the 700-hPa level using a 50-km RMW. The initial analysis provides an updated estimate of the RMW. This updated RMW is then used to readjust data to a common 700-hPa level. A second analysis is then performed for gross error checking to remove potentially erroneous data. A final analysis that uses the updated RMW and the quality controlled data is then created.

The existing flight-level data result in 1466 six-hourly analyses of 177 different TCs. Three well-known and representative examples of the flight-level analyses are shown in Fig. 1. Hurricane Ivan (2004) was a small very

TABLE 2. Data weights for the variational wind analysis as a function of data type and the flight-level wind speed.

Flight-level wind speed (V_{fl}) criteria (kt)	Flight-level tangential and radial wind data weight	SFMR data weight
$V_{fl} \geq 64$	0.175	1.000
$50 < V_{fl} < 64$	$0.500 - (V_{fl} - 50)0.325/14$	$0.350 + (V_{fl} - 50)0.325/14$
$V_{fl} \leq 50$	0.500	0.350

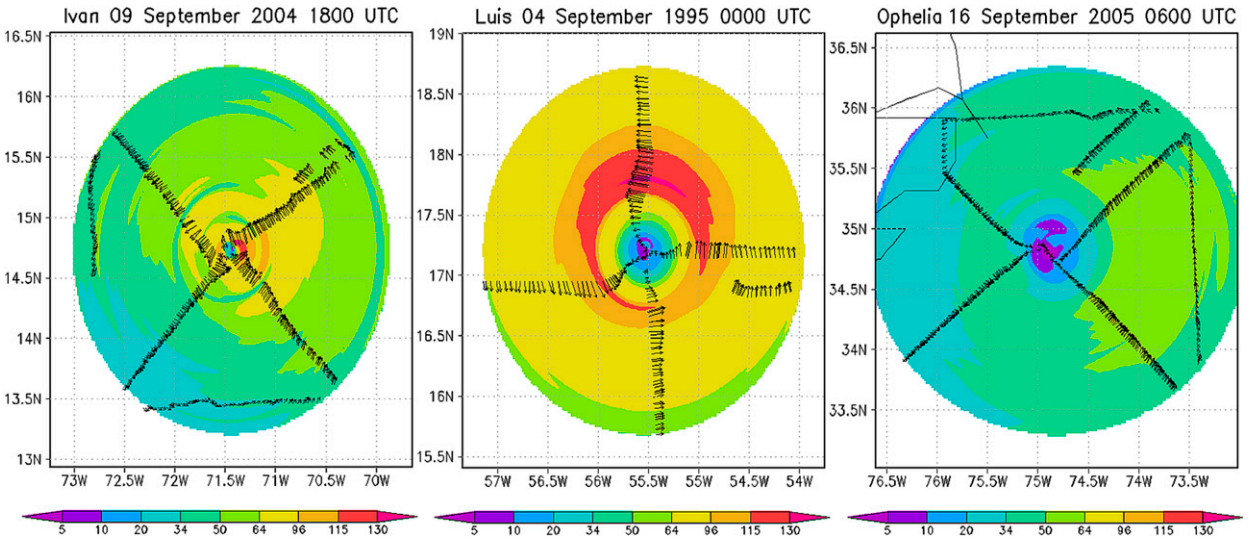

FIG. 1. Examples of flight-level wind speed analyses (kt; color shading). The aircraft-reconnaissance wind vectors, thinned to every 0.05°, are overlaid for comparison. The magnitudes of the vectors correspond to the colors beneath them. Storm names, dates, and times of the examples are shown on the top of each panel.

intense hurricane as it moved through the Caribbean Sea (Franklin et al. 2006), Hurricane Luis (1995) was an annular hurricane (Knaff et al. 2003) with a large wind field located in the eastern Atlantic (Lawrence et al. 1998), and Hurricane Ophelia (2005) was a slow-moving convectively challenged tropical storm off the U.S. east coast (Beven et al. 2008). In the case of Ivan, the storm showed evidence of concentric eyewalls during the compositing time and the analysis captures evidence of a secondary ring of higher winds. The analysis of Luis captures the large RMW and indicates a noticeable asymmetry from northeast to southwest. The Ophelia analysis depicts a very large RMW and a rather slowly radially decaying wind field.

To further simplify the information found in the flight-level polar grids, each wind analysis is decomposed into a direction-relative azimuthal wavenumbers in terms of a normalized amplitude and phase. To account for differences in storm motion, the observed storm direction is used to reorient the wind fields to a common direction, in this case upward or northward, which is also 90° in the x–y plane. Next, the maximum wind speed in the field is used to normalize all other wind speed values. A standard Fourier method is then used to decompose the wind field at each radius into terms of amplitude A and phase P for azimuthal wavenumbers 0, 1, and 2.

The azimuthal (or angular) wavenumber is the number of waves of a given wavelength required to encircle the TC at a given radius. If L is the wavelength and r is the radius, the angular wavenumber k is given by $k = 2\pi r/L$. One can think about wavenumber 0 as the azimuthal mean value, wavenumber 1 as having one maximum and one minimum in the azimuthal domain, etc. Each wavenumber also has a phase shift that allows the wave pattern to rotate in the azimuthal direction. Mathematically, the normalized wind field (NW) at each radius can be represented in a truncated form by $\mathrm{NW}(r) = \mathrm{A0}(r) + \mathrm{A1}(r)\cos[\theta - \mathrm{P1}(r)] + \mathrm{A2}(r)\cos[2\theta - \mathrm{P2}(r)]$, where A0, A1, and A2 are the amplitudes of wavenumber 0, 1, and 2, respectively, and P1 and P2 are the phases associated with wavenumbers 1 and 2. With the wind fields analyzed and decomposed into azimuthal wavenumbers and normalized amplitudes, our focus is now shifted toward accurate estimations of the RMW.

The RMW is arguably one of the most important parameters for estimating the TC wind field as it has a significant effect on the area affected by the strongest winds (Vickery et al. 2009). The RMW along with the radial decay of the wind speed defines many of the important aspects of a TC vortex. In fact, an estimate of the RMW is a required parameter for many hurricane parametric wind models [e.g., those discussed in Depperman (1947), Willoughby et al. (2006), and Wood et al. (2013)] and is a key estimate provided by the Holland (1980) model. Unfortunately, the RMW is also one of the more elusive and difficult parameters to accurately measure without aircraft reconnaissance, aircraft/ground-based radar observations, or conventional observations of chance proximity. As a result, there are relatively few reliable observations of RMW. For this work we endeavor to provide a quality estimate of RMW and will develop climatological relationships to constrain the algorithm developed here.

TABLE 3. The number of cases and means associated with the intensity- (V_{max}) and latitude- (φ) based bins of RMW.

Intensity bins			Latitude bins		
Range	Count	Mean (kt)	Range	Count	Mean (°)
$15 < V_{max} \le 30$	181	25.1	$11.00 < \varphi \le 15.92$	181	14.3
$25 < V_{max} \le 35$	253	30.4	$14.40 < \varphi \le 17.70$	253	16.2
$30 < V_{max} \le 45$	404	37.0	$15.92 < \varphi \le 21.01$	404	18.5
$35 < V_{max} \le 55$	455	44.1	$17.7 < \varphi \le 23.95$	455	20.8
$45 < V_{max} \le 65$	355	54.2	$21.01 < \varphi \le 26.09$	355	23.6
$55 < V_{max} \le 77$	305	65.0	$23.95 < \varphi \le 28.37$	305	26.1
$65 < V_{max} \le 90$	280	76.8	$26.09 < \varphi \le 30.18$	280	28.2
$77 < V_{max} \le 102$	229	88.9	$28.37 < \varphi \le 31.90$	229	30.0
$90 < V_{max} \le 115$	182	101.2	$30.18 < \varphi \le 35.11$	182	32.1
$102 < V_{max} \le 127$	127	112.1	$31.90 < \varphi \le 37.60$	127	34.3
$115 < V_{max} \le 140$	58	123.7	$35.11 < \varphi \le 40.7$	58	36.9
$127 < V_{max} \le 155$	11	136.1	$37.60 < \varphi \le 41.1$	11	40.1
$140 < V_{max} \le 170$	6	145.3	$40.7 < \varphi \le 43.6$	6	42.1

The flight-level wind analyses provided 1466 estimates of the RMW with maximum winds ranging between 15 and 155 kt and latitudes ranging between 11.1° and 43.6° with a radial resolution of 1 km. Several studies have documented the tendency for the RMW to become smaller with increasing intensity (e.g., Weatherford and Gray 1988; Kimball and Mulekar 2004) and to become larger as the TC moves poleward (e.g., Mueller et al. 2006; Kossin et al. 2007). These two factors will be considered in our statistical fit.

To account for the unequal distributions of RMW measurements at various intensities and latitudes, the 1466 estimates were binned by intensity ranges and latitude ranges. The bins for intensity are bounded by the intensity ranges of the Dvorak (1984) current intensity scale. To provide a similar measure of latitudinal variability, the latitudes of each case are binned using the same number of points as the intensity bins, which results in the same number of bins as the intensity stratification but variable latitudinal ranges. Table 3 shows the ranges and number of observations associated with each bin. Figures 2a and 2b show the mean values of RMW associated with the intensity and latitude bins, respectively. These binned results reconfirm that RMW is both a function of intensity and latitude.

Multiple linear regression and quadratic and trigonometric transformations are then used to develop the best fit of the binned data. The best fit involves the intensity V_{max}, intensity squared, and intensity cubed along with the cosine of the latitude φ as shown in (1):

$$\mathrm{RMW} = 218.3784 - 1.2014V_{max} + \left(\frac{V_{max}}{10.9844}\right)^2 - \left(\frac{V_{max}}{35.3052}\right)^3 - 145.5090\cos\varphi. \quad (1)$$

Figure 2c shows the regressed result on the dependent binned values of intensity and latitude. This relationship defines the RMW climatology, which depicts a nearly linear and one-to-one relationship that explains almost all of the variance in the average–binned data. Figure 2d shows the climatological relationship applied to the individual RMW estimates, which shows the scatter about climatology—explaining a third of the variance.

To provide independent estimates of RMW and to test the climatological RMW estimates developed here, historical RMW estimates made from surface, aircraft, and radar observations in the Atlantic and western North Pacific have been digitized from Ho et al. (1975) and Schwerdt et al. (1979). Figure 3 shows the climatological RMW versus the RMW in the Atlantic and RMW estimates based on eye radius in the western North Pacific.[1] These independent results show that this climatological relationship explains one-third of the variance in the Atlantic record and 17% of the variance in the less accurate western Pacific record.[2] Also note that the sample mean latitudes are 29.2° and 21.3° for the Atlantic and western Pacific samples, respectively, which explains the smaller predicted and observed RMW values in the western Pacific sample. From this analysis it seems justified to use the prognostic factors in (1) as potential predictors for the

[1] RMW is estimated in the western Pacific using the best fit shown in Shea (1972, his Fig. 26) or RMW = R_{eye} + minimum [14, (170 − V_{max})0.12], where R_{eye} is the eye radius in nautical miles and V_{max} is the intensity in knots.

[2] It is noteworthy that western North Pacific RMW estimates were based on radar eye-based radii times a factor of 1.25 for all intensities (Schwerdt et al. 1979), which makes these estimates less accurate.

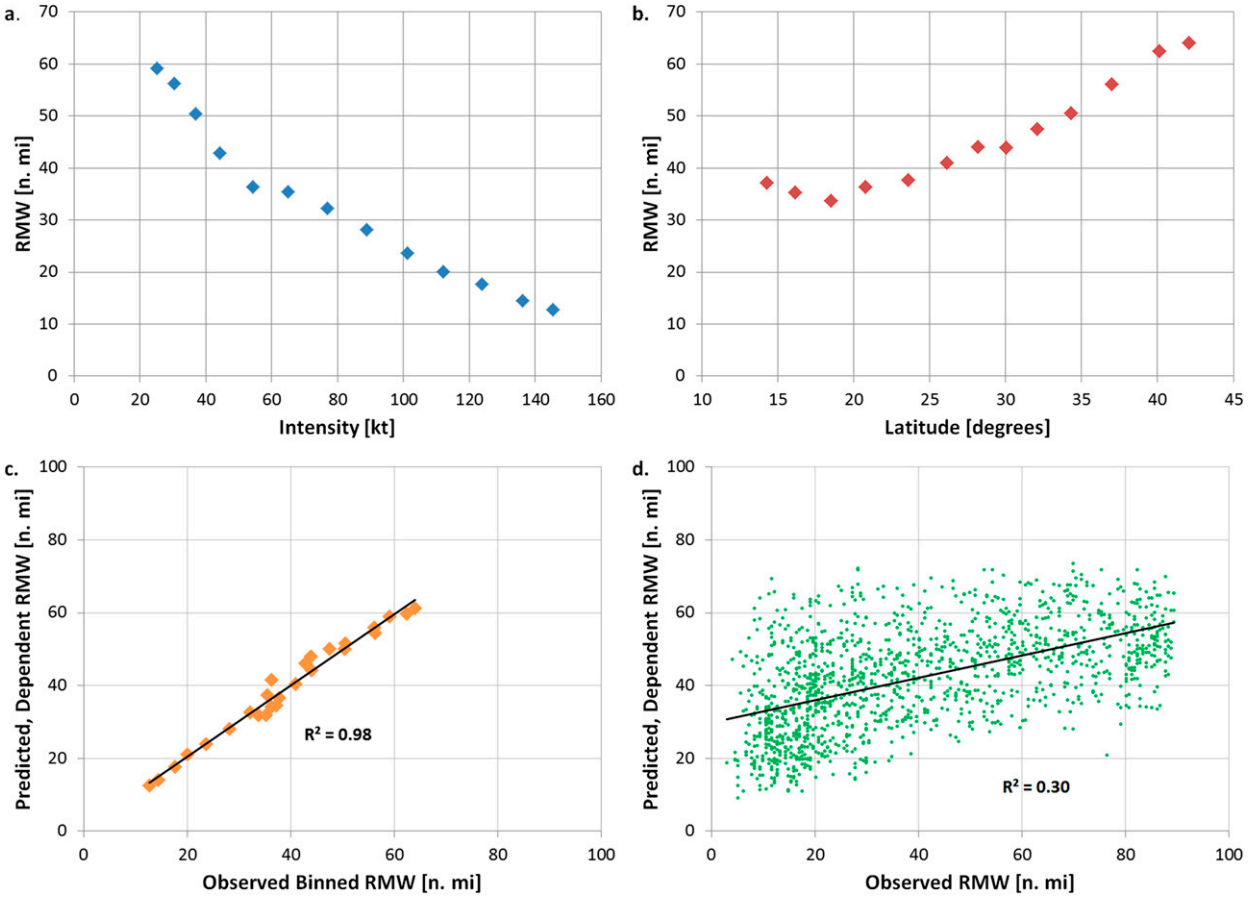

FIG. 2. RMW binned as a function of (a) intensity and (b) latitude. (c) The dependent comparison of observed and predicted values of RMW based on the binned averages, and (d) the dependent comparison of climatological RMW vs observed RMW from aircraft-based analyses. The goodness of fit is measured by the regression coefficient squared, which is provided for (c) and (d). RMW units are nautical miles.

estimation of flight-level winds to help constrain the estimated RMW.

The other diagnostic information used in this study comes from IR satellite imagery contained in an archive maintained at the NOAA Regional and Mesoscale Meteorology Branch, which is collocated with the Cooperative Institute for Research in the Atmosphere (CIRA) at Colorado State University. The IR imagery archive is referred to as the CIRA IR archive hereinafter and has been described in Mueller et al. (2006), Zehr and Knaff (2007), and Knaff et al. (2014).

The CIRA IR archive and the best-track data were used to create storm-centered IR imagery that had been remapped onto a polar grid and rotated with respect to motion. The polar grid has a 4 km × 10° resolution and extends to a radius of 602 km as described in Knaff et al. (2014). From this imagery a principal component analysis was performed on the covariance matrix of brightness temperatures. The normalized spatial loading factors or empirical orthogonal functions (EOFs) associated with the first 12 principal components (PCs) are shown in Fig. 4. Table 4 provides the variance explained and interpretation of each of these PCs. Twelve PCs were kept for algorithm development to allow the potential of capturing the secondary wind maxima and higher wavenumbers in the wind field. To this end, notice (Fig. 4) that the 1st, 4th, 9th, 11th, and 12th PCs contain what appear to be generally symmetric PCs explaining the radial wavenumbers 0, 1, and 2. The second and third PCs project onto the azimuthal wavenumber 1, whereas the remaining higher-order PCs explain larger azimuthal wavenumbers.

With the input data readied, the focus now shifts to algorithm development. However, there is one preparatory step needed to allow for the estimation of winds beyond the 165-km analysis domain. This is accomplished by adding a single azimuthally averaged tangential wind at a radius of 500 km as an outward wind speed anchor. The azimuthally averaged tangential wind at 850 hPa is calculated from NOAA's Global Forecast

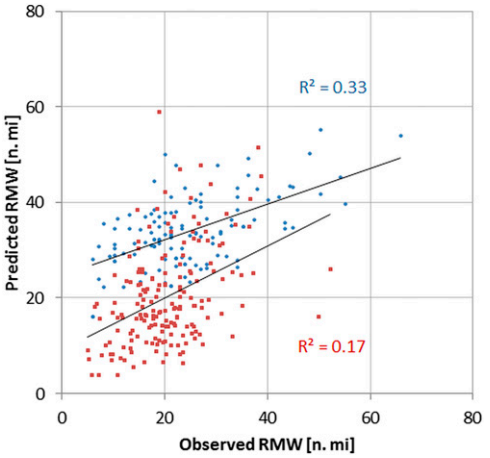

FIG. 3. Independent comparison of RMW vs predicted climatological value of RMW [i.e., (1)]. Blue points are valid in the North Atlantic and come from Ho et al. (1975), and red points come from the western North Pacific in Schwerdt et al. (1979) and are calculated from observations of eye radius following a relationship found in Shea (1972) and provided in the text.

System (GFS) analyses, is contained in the Statistical Hurricane Intensity Prediction Scheme (DeMaria et al. 2005) developmental database, and is adjusted to 700 hPa using the same methodology as for the flight-level data. This 500-km tangential wind provides important information about the overall size of the TC vortex, as demonstrated in Knaff and Zehr (2007) and discussed further in Knaff et al. (2014). Note that the 500-km tangential wind speed is treated as being entirely composed of azimuthal wavenumber 0.

The SFPCA method is then used to relate the motion-oriented, two-dimensional wind field to two-dimensional features in the IR imagery. In SFPCA, principal components of one field are correlated with the amplitude of another. In this study, IR PCs, and parameters related to the climatological RMW (i.e., intensity, latitude, and translation speed) are regressed onto the normalized amplitudes and phases of the wavenumber 0–2 wind field at radii from 1 to 165 km and one GFS-based tangential wind estimate at 500 km. This procedure collectively is referred to as SFPCA hereinafter.

To generate a wind field from the resulting SFPCA regression equations, the maximum intensity, storm translation speed, storm direction, and the first 12 normalized principal components are needed. From these inputs, normalized amplitudes and phases associated with azimuthal wavenumber 0–2 are estimated. The amplitudes and phases at radii from 1 to 165 km are then smoothed using a simple binomial filter. Next a cubic spline is applied to the amplitude and phase fields to make estimates from 165- to 500-km radius, noting that the amplitudes and phases of wavenumbers 1 and 2 at 500 km are zero. The observed maximum wind (from best track or operational source) is adjusted to flight level and multiplied by the normalized amplitudes. Finally, since the output from the algorithm is typically unable to predict a normalized wind field with a value of 1, a bias correction is needed. To allow the wind reconstruction to capture the maximum wind, an exponentially decaying bias correction is applied to a small region surrounding the maximum normalized wind estimate, which is bias corrected to a value of 1.0. The normalized flight-level winds are then estimated on a polar grid using the amplitudes and phases at each radii. The observed flight-level wind (based on the observed intensity) is then multiplied by the normalized flight-level wind to estimate the wind speeds. Finally, the wind field is rotated to the observed storm heading.

3. Results

a. *Algorithm details*

The first results examined are those related to measures of goodness of fit. Figure 5 shows the multiple regression coefficients R^2 associated with each vortex parameter (A0, A1, A2, P1, and P2) as a function of radius. The R^2 metric is a measure of the percentage variance explained by the SFPCA-based equations, which is a measure of goodness of the fit ranging from 0 to 1.

Results for the SFPCA indicate that A0, A1, and A2 are statistically related to the factors used in the regression, especially beyond 75 km. The azimuthal mean conditions (A0) best explain the variability within 50 km. Beyond 50 km, A1 and A2 show R^2 values that are more similar to those of A0. This implies that the algorithm produces the largest azimuthal wavenumber 1 and 2 asymmetries beyond 50 km, noting here that the magnitudes of A1 and A2 are on average about 30% and 12% of the magnitude of A0, respectively.

P1 and P2 proved to be much harder to predict. The R^2 values associated with P1 are on the order of 8%–10% and are much smaller for P2. This poor predictability of P2 was validated by results not shown here, which indicate the inclusion of A2 and P2 degraded the estimates of the overall wind field. For this reason, the wind reconstruction discussed hereinafter will be constrained to the azimuthal wavenumber 0 and 1 contributions.

To provide the reader with an idea of what factors are most important for the SFPCA, Fig. 6 provides the normalized regression coefficients that are most important and/or informative to the estimates of A0, A1, and P1. The colors of each of the dependent variables and ranges are consistent from panel to panel.

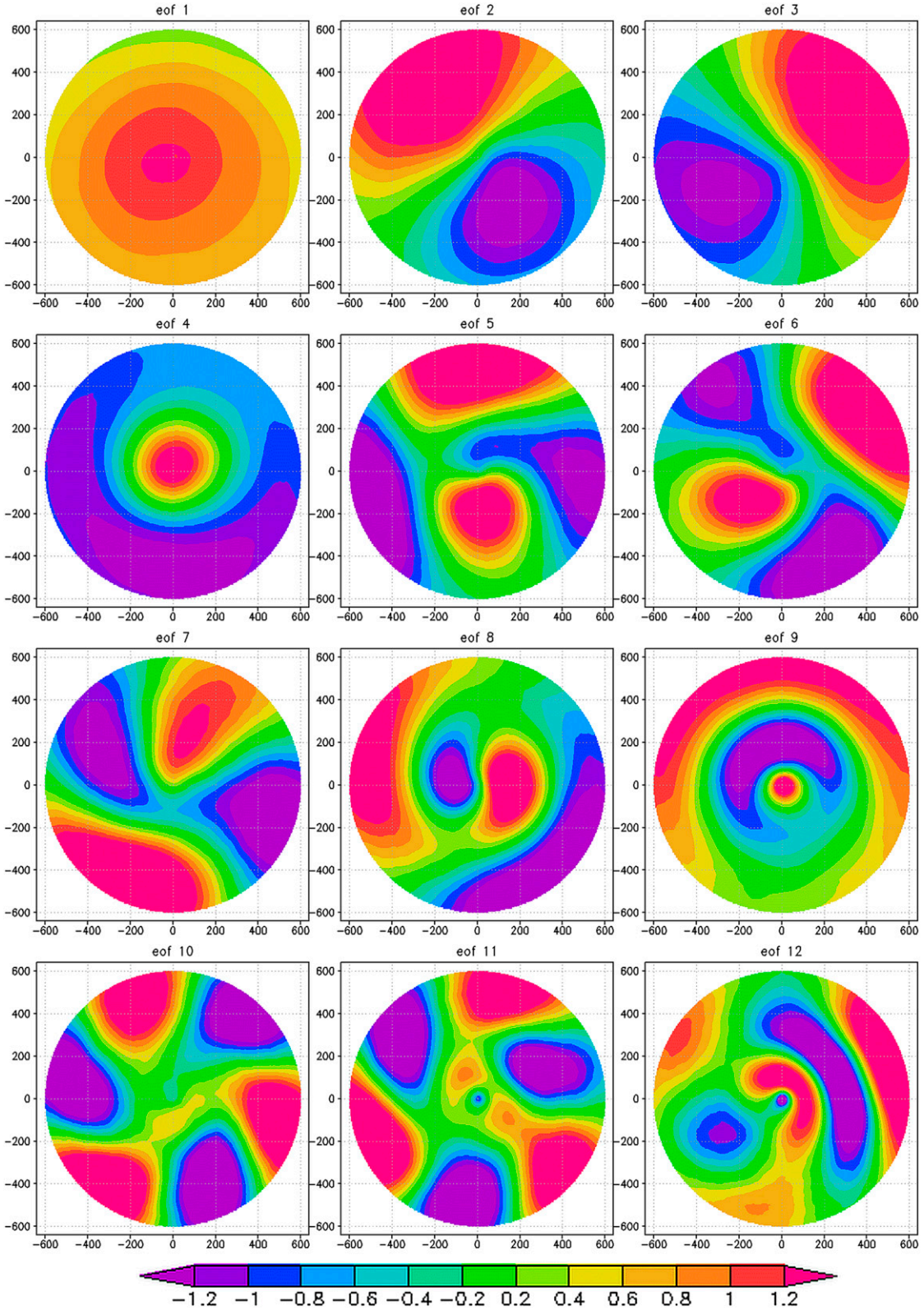

FIG. 4. The normalized loadings (EOFs) associated with the PCs associated with direction-relative and storm- centered IR images of TCs. The TC translation direction is toward the top of the page.

TABLE 4. Percent variance explained by the EOFs shown in Fig. 4 and their associated PCs.

IR EOF/PC	Interpretation	Percent variance explained
1	Size/intensity of the cloud shield	32.2
2	Azimuthal wavenumber 1	11.5
3	Azimuthal wavenumber 1	10.7
4	Symmetric pulsing variability	8.9
5	Azimuthal wavenumber 2	2.9
6	Azimuthal wavenumber 2	2.8
7	Azimuthal wavenumber 2	2.7
8	Azimuthal wavenumber 2 + radial wavenumber 1	2.4
9	Radial wavenumber 1	2.4
10	Azimuthal wavenumber 3	1.0
11	Azimuthal wavenumbers 2 and 3 + radial wavenumber 2	1.0
12	Azimuthal wavenumbers 2 and 3 + radial wavenumber 2	0.9

The top two panels in Fig. 6 show the normalized regression coefficients associated with A0, with climatological RMW factors on the left and IR PCs to the right. Notice that A0 is best explained by the climatological RMW factors, particularly those related to the intensity (V_{max}, V^2_{max}, and V^3_{max}) shown in the top-left panel in Fig. 6, and the more symmetric IR PCs (1, 4, 9, 11, and 12) shown in the top-right panel. One noteworthy item is that larger values of cosine of latitude (i.e., lower latitude) lead to higher winds toward the center or smaller storms.

Similarly, the normalized regression coefficients associated with A1 are shown in the second pair of panels in Fig. 6. Here, again, the factors related to intensity are most important to A1, but in this case IR PCs 2, 3, 4, and 9 also appear to be relatively important. Increased storm speed is shown to result in larger values of A1. Referring back to Fig. 4, PCs 2 and 3 are related (as a pair) to the wavenumber 1 variations of the IR scene, which are related to a number of environmental factors including storm translation and vertical wind shear. The structures of PCs 4 and 9, combined together, provide information about the existence and radial structure of an eye scene in the imagery.

The regressions associated with P1 in the third pair of panels (Fig. 6) indicate that variations in intensity and PCs 2 and 3 are most important for estimating P1, again suggesting the importance of asymmetries in the wavenumber 1 cold cloud asymmetries. Somewhat surprising is the poor relationship with storm speed, which is shown for completeness. Thus, the rotation of wavenumber 1 asymmetries in this algorithm primarily results from changes in intensity and asymmetries in the IR imagery.

One of the primary justifications for developing this algorithm was to better depict the wind asymmetries. We now show in an idealized sense how the wavenumber

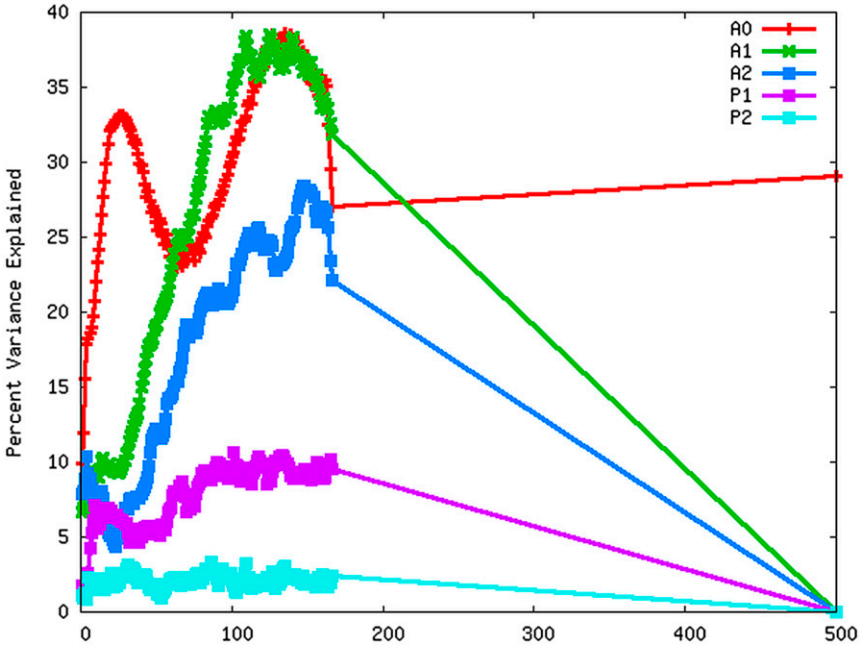

FIG. 5. The R^2 or percent variance explained for the amplitudes and phase of wavenumbers 0–2 of the wind field as a function of radius.

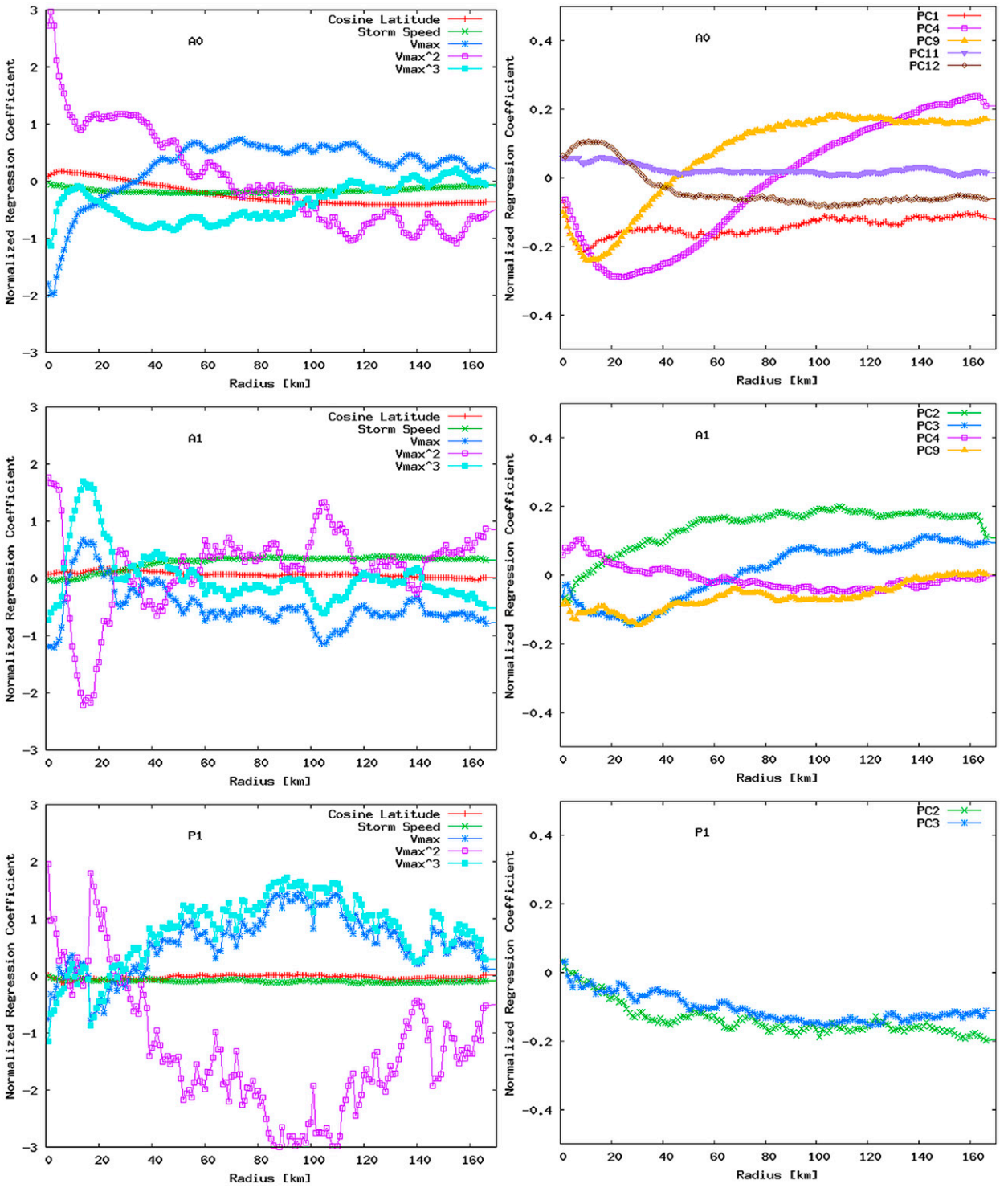

FIG. 6. The normalized regression coefficients associated with the amplitudes and phases of azimuthal wavenumbers 0 and 1 of the wind field. Those parameters that make the most important contribution and those that provide interpretive information are provided. Information is shown in each pair of panels with climatological RMW factors on the left and PC contributions on the right. These pairs show the normalized regression coefficients for A0, A1, and P1 descending from the top to the bottom of the figure. Line colors are consistent between panels.

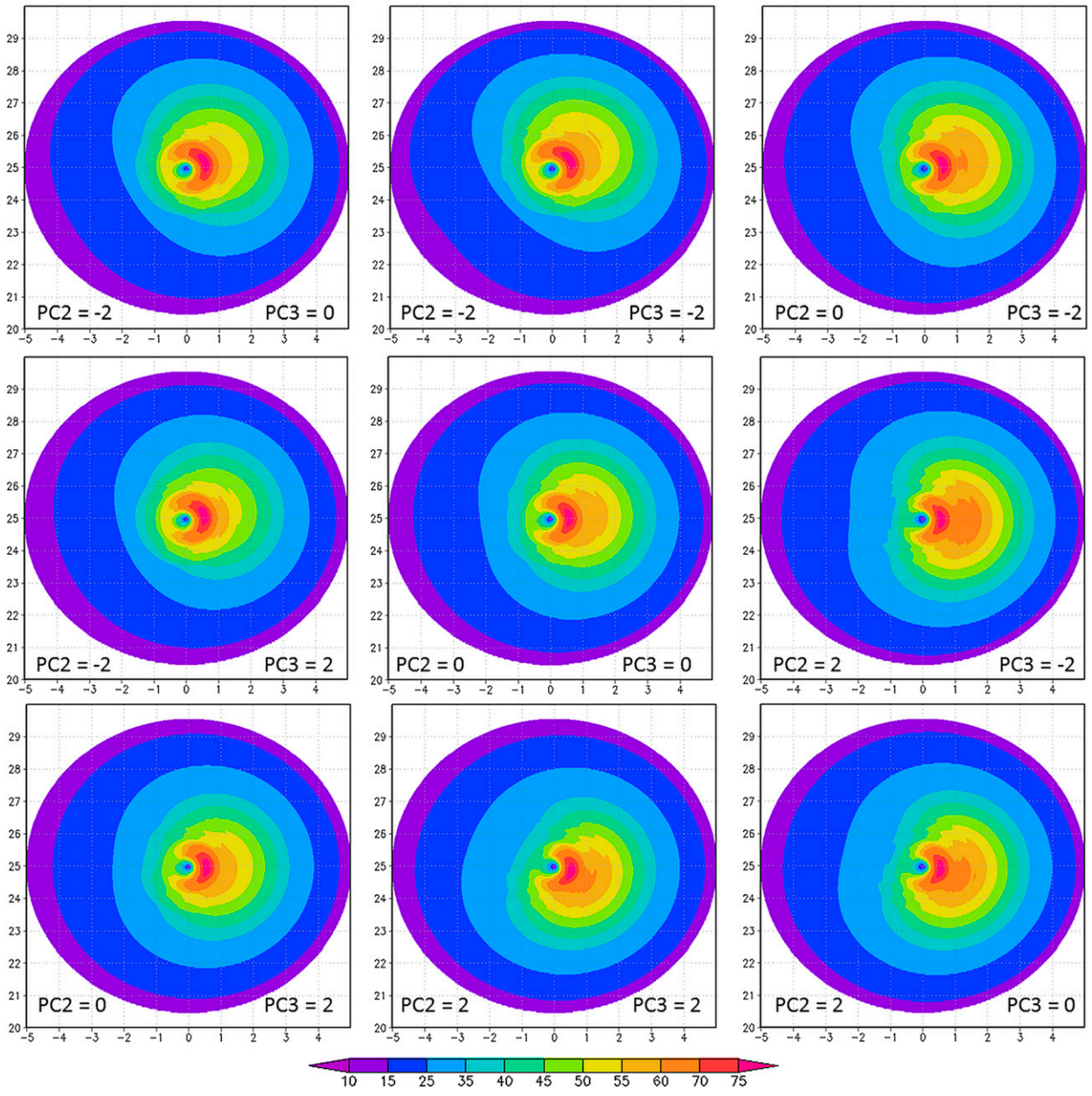

FIG. 7. Nine idealized flight-level wind depictions produced by the SFPCA. The idealized TC is located at 25°N, 0°; has an intensity of 65 kt (33.41 m s^{-1}); and is moving northward at 10 kt (5.14 m s^{-1}). The IR PCs 4–12 have a fixed value of 0.0, and PC 1 has a value of −2.0. PCs 2 and 3 are allowed to vary to produce azimuthally varying IR asymmetries. The nine panels are oriented in the same manner as the cold IR asymmetries produced by the variation of PCs 2 and 3. Wind speeds are provided by the shaded contours (kt). The maximum contour in all plots is 75 kt.

1 asymmetries of IR brightness temperatures (i.e., PCs 2 and 3) change the predicted wind field. In this case the idealized TC has an intensity of 65 kt, has a northward movement of 10 kt, and is located at 25°N and 0°, PC 1 is equal to −3.0 (a large storm), PCs 4–12 are all set to a value of 0, and only PCs 2 and 3 are allowed to vary. Figure 7 shows nine possible combinations of convective asymmetries represented by values of PCs 2 and 3. Each panel is located where the cold cloud tops would be situated relative to the center panel. For instance, PC 2 = −2 and PC 3 = 0 is the case in which wavenumber 1 cloud tops are coldest in the left-front quadrant of the idealized storm. Notice how the wind asymmetries, particularly at larger radii, mimic the convective asymmetries when the cold IR asymmetries are located in the front, rear, or right side of the system (e.g., right column

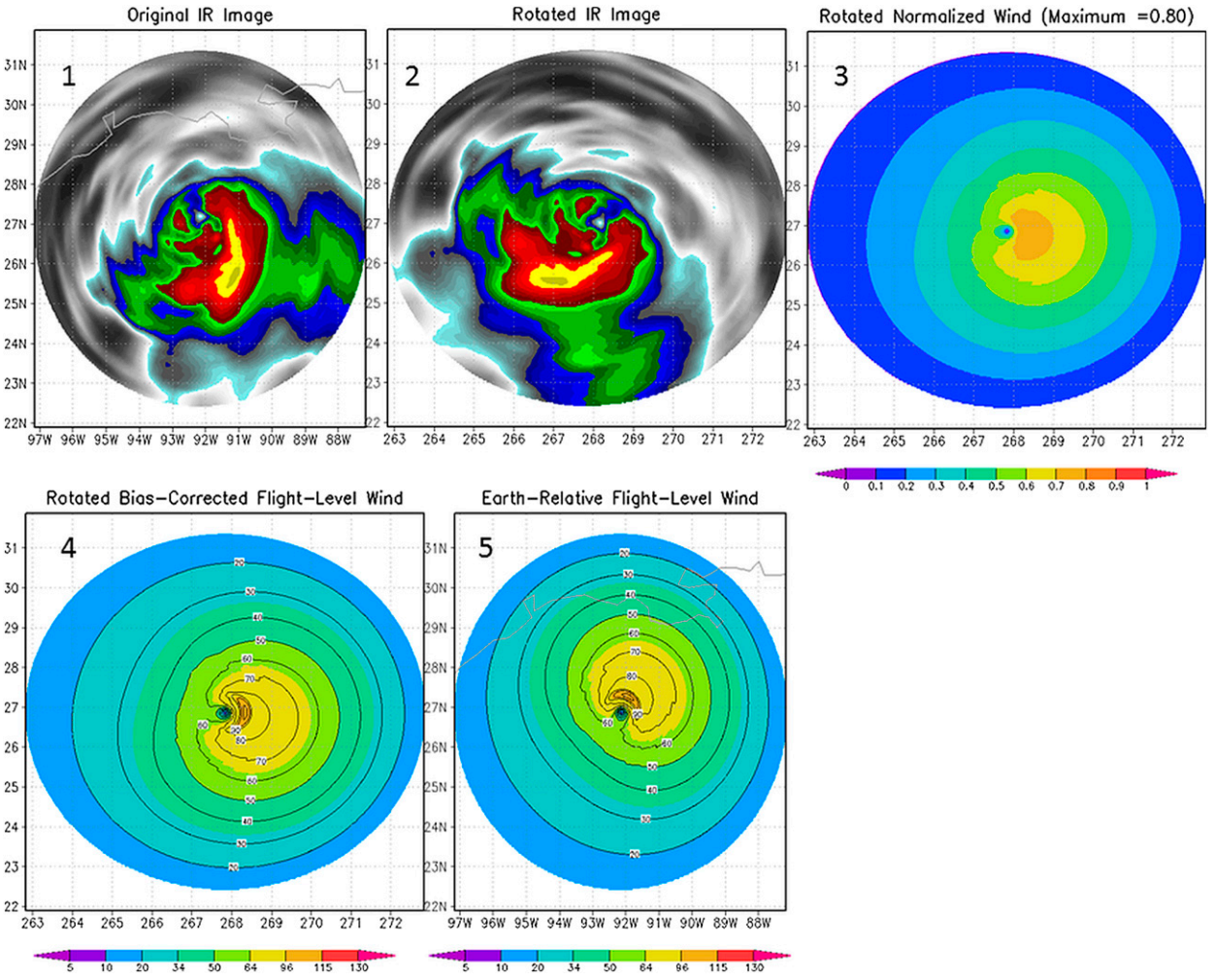

FIG. 8. An illustration of the steps taken to estimate the wind field. The progression is from left to right and then top to bottom. Imagery is mapped to a polar grid (step 1) and then rotated with respect to direction (step 2). Rotated imagery (via PCs), translation speed, latitude, and intensity are then used to estimate the normalized wind field (step 3). The observed intensity is then applied to create a wind speed field (step 4). Last, the wind field is rotated back to its Earth-relative directional component (step 5). This case is from Hurricane Ike (2008) at 1145 UTC 12 Sep.

in Fig. 5). Cold cloud asymmetries on the left side of the storm appear to result in more symmetry in the wind field (e.g., left column in Fig. 5). The region of the maximum winds also appears to move from the right-front region to the right-rear region as cloud-top temperature asymmetries move from the front (PC 2 = −2 and PC 3 = −2) to the rear portion of the storm (PC 2 = 2 and PC 3 = 2). These results are consistent with other observational and modeling studies where weak and moderate ($<15\,m\,s^{-1}$) vertical wind shear results in downshear and left convective asymmetries in the rainband region (e.g., Corbosiero and Molinari 2003; Chen et al. 2006; Reasor et al. 2013) and surface wind asymmetries that are generally to the right of motion and rotated in the downshear direction (Ueno and Bessho 2011; Uhlhorn et al. 2014). In a similar manner, this algorithm can also predict variations of vortex size and radial structure including the RMW using the variations of the symmetric IR PCs, namely PCs 1, 4, and 9, but this result is not illustrated for brevity.

To summarize, the SFPCA-based algorithm uses the observed intensity, storm translation speed, and 12 IR PCs to predict the wind field in terms of A0, A1, and P1 at each radii. Much of the basic vortex structure is described by factors related to the storm intensity and motion. This basic vortex structure is modified by information provided by IR imagery that allows for variations in the size, radial structure, and location and strength of wavenumber 1 asymmetries. Following the steps provided at the end of section 2, a wind field can

TABLE 5. Wind field statistics stratified by flight-level intensity categories and based on dependent data. Shown are the number of cases used in each sample along with the bias, MAE, RMSE, and R^2.

Intensity	No.	Bias (kt)	MAE (kt)	RMSE (kt)	R^2
TD	76	−0.06	4.87	6.31	0.28
TS	530	0.22	6.77	8.69	0.48
nMH	387	0.06	9.99	12.79	0.49
MH	371	0.17	13.00	16.50	0.53
All H	758	0.12	11.46	14.77	0.59
All cases	1364	0.15	9.27	12.38	0.72

then be estimated. To help better visualize the steps involved, Fig. 8 shows an example of the input and output of this algorithm for Hurricane Ike (2008) as it approached the Texas coast.

b. Validation

An important aspect of estimating the wind field is validation. Previous methods, namely those of M06 and K07, provide a baseline upon which this study desires to improve. However, since the developmental dataset, domain, and validation data are different, it is difficult to make one-to-one comparisons. Nonetheless, the method of M06 provided mean absolute error estimates of 9.85 and 10.40 kt and percent variance explained values of 26% and 54% for dependent (1995–2003) and independent cases (2004), respectively, for the total flight-level wind field. K07 compared their results with azimuthally averaged wind profiles and found maximum mean absolute errors (MAE) on the order of 10 kt (cf. their Fig. 7).

The method presented here has dependent (i.e., those based on the dependent statistical fits) MAE values that are slightly higher than the results in either the M06 or K07 studies, but it is important to realize that the analysis used in this study has higher spatial resolution and contains more variability (a good thing) than the relatively smooth analyses used in the M06 and K07 studies. Table 5 presents the dependent statistics stratified by wind field maximum winds (intensity) based on the reconstructed wind field based upon wavenumbers 0 and 1. Categories of the flight-level intensity include tropical depressions (TDs; $v < 34$ kt), tropical storms (TSs; 34 kt $\leq v < 64$ kt), nonmajor hurricanes (nMHs; 64 kt $\leq v <$ 96 kt), major hurricanes (MHs; $v \geq 96$ kt), and all hurricanes (all H; $v \geq 64$ kt). Since this method minimizes the errors associated with the amplitudes and phases of the wind field and not the wind field itself, there are small (<1 m s^{-1}) biases resulting from the dependent validation. Overall, the MAEs and root-mean-square errors (RMSE) are comparable to previous studies when all cases are considered. In general, the correlation between predicted and observed wind fields increases with intensity (i.e., organization), while the errors increase with increasing intensity.

The same statistics were calculated for the M06 method modified as explained in the appendix of Knaff et al. (2011). Those statistics can then be compared with the more-detailed flight-level analyses used in this study. All bias, MAE, and RMSE statistics from this new method improved upon those produced by the modified M06 method in a statistically significant way. For instance, RMSEs associated with the modified M06 method were 8.53, 11.20, 14.55, 18.33, 16.57, and 14.39 kt, for TD, TS, nMH, MH, all H, and all cases, which are all larger in a statistically significant way than the values shown in Table 5. The R^2 statistics from the new method were also larger for most flight-level intensity stratifications.

To provide the reader some idea of where this method may produce the largest errors, Fig. 9 shows the average wind field (contours) and MAEs (shaded) for cases with flight-level winds of TS, nMH, and MH strength. The largest errors are found along the inner edge of the radius of maximum wind (magenta contours) where the wind speed gradient is typically largest. This result is somewhat expected because of errors in estimating the exact RMW. Spatial biases (not shown) suggest that the estimate of the RMW is generally too small and the maximum wind is typically too high on the right side of the circulation and too low at the rear of the circulation. The largest biases are again located inside the observed RMW. This underestimate of the RMW is similar to the results presented in K07 (which also uses SFPCA) yet unlike results found in M06, where RMW were often overestimated.

The ability of this method to estimate secondary wind maxima was also examined but not shown. Findings suggest that this method cannot estimate secondary wind maxima as defined in the literature (e.g., Kossin and Sitkowski 2009). While this new method can produce secondary wind maxima per say, those maxima fail to meet the criteria listed in the literature as the minimum wind speed located between the primary and secondary maxima is not that different from either maximum. So it appears that this method cannot resolve the observed secondary wind maxima, but rather will produce a wider region of more intense winds when multiple wind maxima could be present.

4. Summary and future work

In this paper, a new method for estimating tropical-cyclone flight-level winds using operationally available information and routine IR satellite imagery is presented.

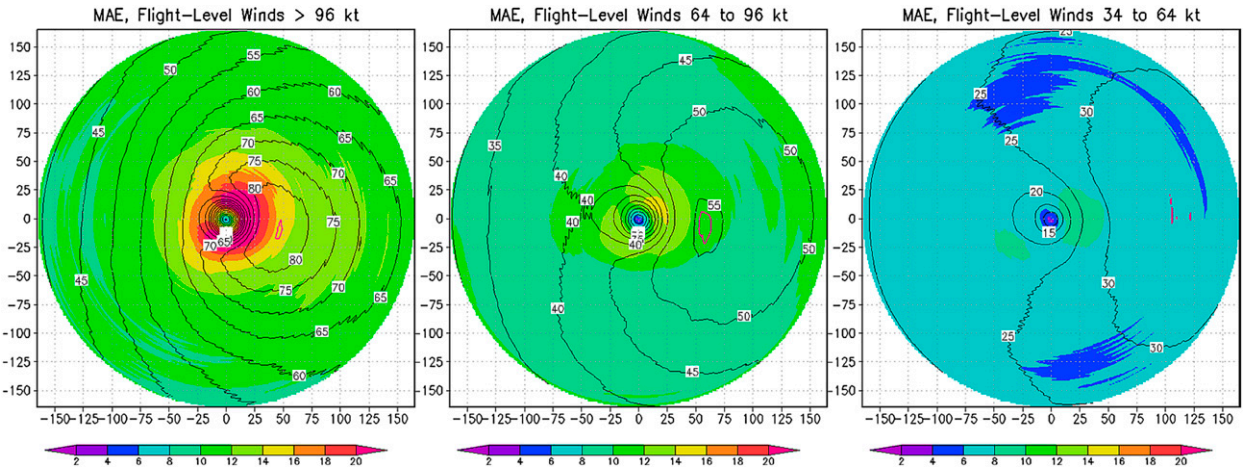

FIG. 9. Dependent mean wind field (contours) and MAEs (color shading) stratified by flight-level analysis winds with cases having winds (left) >96 kt, (middle) between 64 and 95 kt, and (right) between 34 and 64 kt. Note that the motion of the composite errors is toward the top of the page. The largest errors are found inside the RMW where the gradients in wind speed are the largest. The magenta contour in each panel shows where the average RMW of flight-level wind is located in each composite. The scale is the same for all panels.

Previous methods had relied on less detailed developmental data and ignored variations of the wavenumber 1 azimuthal wind asymmetries. Several steps were taken to improve upon existing methods including 1) using several more years of aircraft reconnaissance data; 2) creating a higher-resolution wind analysis system for the developmental wind fields, one that can better depict the radial and azimuthal variations of the winds (examples shown in Fig. 1); and 3) statistically relating two-dimensional IR information (i.e., PCs) to the amplitude and phase of wavenumbers 0, 1, and 2 of the TC wind field on a TC-motion-relative polar analysis grid.

The algorithm developed is based on an SFPCA methodology and uses spatial IR information contained in PCs along with current storm conditions that are related to variations of the climatological RMW, which were reexamined as part of this work (Figs. 2 and 3). The inclusion of IR PCs (patterns shown in Fig. 4) allows for radial and azimuthal variations (explicitly shown in Fig. 7) of the wind field beyond the mean vortex related to the current storm conditions (storm intensity, storm motion, and storm latitude).

Results based on the dependent statistical analysis indicate that this methodology can estimate the flight-level winds accurately, but that incorporating the predicted wavenumber 2 information degrades the prediction of the wind field. Dependent error analysis of the reconstructed wind speeds based on predicted wavenumbers 0 and 1 shows that errors increase as a function of intensity (Table 5) and that the largest errors are located on the inner edge of the radius of maximum winds (Fig. 9). Field correlations also generally increase with intensity, but the largest field correlations were found when all cases were combined.

This method is also shown to be statistically superior to the modified Mueller et al. (2006) method that is used in the NESDIS MTCSWA (Knaff et al. 2011). This implies that MTCSWA can be improved by using this new method. The same methods used to bring the aircraft wind data to a common pressure level in this study could also be used in the MTCSWA, representing another significant improvement. The current version of MTCSWA applies a constant inflow angle of 20° to the analyzed flight-level wind vectors. Since that time, Zhang and Uhlhorn (2012) have conducted a comprehensive study of inflow angles from dropwindsonde records. Their findings show similar mean inflow, but also indicate significant variation of inflow as a function of storm motion, RMW, intensity, and azimuth around the storm. This formulation of inflow angles could be used to further improve satellite-reconnaissance-based surface wind estimates.

Future work will continue to focus on improving the use of routine satellite reconnaissance to diagnose TC structure. A number of efforts to do so are under way. For instance, this methodology and aircraft-based wind field dataset are being applied to microwave imagery. Additionally, since this method can be applied to any IR image, relatively high temporal resolution wind estimates are possible and may help us to better understand and diagnose rapid TC structure. Since routine Dvorak intensity fixes, whether subjective (Dvorak 1984) or objective (Olander and Velden 2007), rely on a single IR image, work has started to use this and other IR-based techniques (e.g., Knaff et al. 2014) to provide wind structure estimates consistent with Dvorak fix intensity

estimates. Furthermore, to reduce the reliance on aircraft-reconnaissance-based wind analyses and because the model provides complete coverage of winds at multiple levels, a study that uses high-resolution hurricane model wind fields and accompanying synthetic IR imagery in place of the observation-based developmental data used here is also being explored. One possible outcome of that work is that such algorithms could serve as a method to initialize model TC vortices (using the observed IR imagery).

Although the wind field estimates from the algorithm developed here respond to IR asymmetries, there still remains a need to study the relationships between vertical wind shear and asymmetries in both the TC wind fields and IR imagery. This is a topic of future work. Such work will lead not only to better scientific understanding but to improved operational products.

The method presented here along with improved methods to reduce flight-level winds at the surface and to estimate surface inflow angles is currently being proposed as a way of improving the NESDIS MTCSWA product, and the development of an experimental, real-time display of these capabilities is under way.

Acknowledgments. This research was supported by a number of NOAA programs, including the GOES-R Risk Reduction Program, the Hurricane Forecast Improvement Program, and the Joint Hurricane Testbed under a NOAA grant (NA17RJ1228). The authors also thank Buck Sampson, Chris Velden, and the other two anonymous reviewers for their constructive comments and suggestions. The views, opinions, and findings contained in this report are those of the authors and should not be construed as an official National Oceanic and Atmospheric Administration or U.S. government position, policy, or decision.

REFERENCES

Beven, J. L., II, and Coauthors, 2008: Atlantic hurricane season of 2005. *Mon. Wea. Rev.,* **136,** 1109–1173, doi:10.1175/2007MWR2074.1.

Bretherton, C. S., C. Smith, and J. M. Wallace, 1992: An intercomparison of methods for finding coupled patterns in climate data. *J. Climate,* **5,** 541–560, doi:10.1175/1520-0442(1992)005<0541:AIOMFF>2.0.CO;2.

Chen, S. S., J. A. Knaff, and F. D. Marks Jr., 2006: Effects of vertical wind shear and storm motion tropical cyclone rainfall asymmetries deduced from TRMM. *Mon. Wea. Rev.,* **134,** 3190–3208, doi:10.1175/MWR3245.1.

Corbosiero, K. L., and J. Molinari, 2003: The relationship between storm motion, vertical wind shear, and convective asymmetries in tropical cyclones. *J. Atmos. Sci.,* **60,** 366–376, doi:10.1175/1520-0469(2003)060<0366:TRBSMV>2.0.CO;2.

DeMaria, M., M. Mainelli, L. K. Shay, J. A. Knaff, and J. Kaplan, 2005: Further improvements in the Statistical Hurricane Intensity Prediction Scheme (SHIPS). *Wea. Forecasting,* **20,** 531–543, doi:10.1175/WAF862.1.

Depperman, R. C. E., 1947: Notes on the origin and structures of Philippine typhoons. *Bull. Amer. Meteor. Soc.,* **28,** 399–404.

Dvorak, V. F., 1984: Tropical cyclone intensity analysis using satellite data. NOAA Tech. Rep. 11, 45 pp. [Available from NOAA/NESDIS, NOAA Center for Weather and Climate Prediction, 5830 University Research Ct., College Park, MD 20740.]

Franklin, J. L., M. L. Black, and K. Valde, 2003: GPS dropwindsonde wind profiles in hurricanes and their operational implications. *Wea. Forecasting,* **18,** 32–44, doi:10.1175/1520-0434(2003)018<0032:GDWPIH>2.0.CO;2.

——, R. J. Pasch, L. A. Avila, J. L. Beven, M. B. Lawrence, S. R. Stewart, E. S. Blake, 2006: Atlantic hurricane season of 2004. *Mon. Wea. Rev.,* **134,** 981–1025, doi:10.1175/MWR3096.1.

Ho, F. P., R. W. Schwerdt, and H. V. Goodyear, 1975: Some climatological characteristics of hurricanes and tropical storms, Gulf and east coasts of the United States. NOAA Tech. Rep. NWS 15, 87 pp. [Available online at http://www.gpo.gov/fdsys/pkg/CZIC-qc851-u65-no-15/content-detail.html.]

Holland, G. J., 1980: An analytic model of the wind and pressure profiles in hurricanes. *Mon. Wea. Rev.,* **108,** 1212–1218, doi:10.1175/1520-0493(1980)108<1212:AAMOTW>2.0.CO;2.

Kimball, S. K., and M. S. Mulekar, 2004: A 15-year climatology of North Atlantic tropical cyclones. Part I: Size parameters. *J. Climate,* **17,** 3555–3575, doi:10.1175/1520-0442(2004)017<3555:AYCONA>2.0.CO;2.

Klotz, B. W., and E. W. Uhlhorn, 2010: Stepped Frequency Microwave Radiometer algorithm improvements addressing rain contamination of surface wind speed measurements in tropical cyclones. *29th Conf. on Hurricanes and Tropical Meteorology,* Tucson, AZ, Amer. Meteor. Soc., 13B.6. [Available online at https://ams.confex.com/ams/pdfpapers/167846.pdf.]

Knaff, J. A., and R. M. Zehr, 2007: Reexamination of tropical cyclone wind–pressure relationships. *Wea Forecasting,* **22,** 71–88, doi:10.1175/WAF965.1.

——, J. P. Kossin, and M. DeMaria, 2003: Annular hurricanes. *Wea. Forecasting,* **18,** 204–223, doi:10.1175/1520-0434(2003)018<0204:AH>2.0.CO;2.

——, M. DeMaria, D. A. Molenar, C. R. Sampson, and M. G. Seybold, 2011: An automated, objective, multisatellite platform tropical cyclone surface wind analysis. *J. Appl. Meteor. Climatol.,* **50,** 2149–2166, doi:10.1175/2011JAMC2673.1.

——, S. P. Longmore, and D. A. Molenar, 2014: An objective satellite-based tropical cyclone size climatology. *J. Climate,* **27,** 455–476, doi:10.1175/JCLI-D-13-00096.1.

Kossin, J. P., and M. Sitkowski, 2009: An objective model for identifying secondary eyewall formation in hurricanes. *Mon. Wea. Rev.,* **137,** 876–892, doi:10.1175/2008MWR2701.1.

——, J. A. Knaff, H. I. Berger, D. C. Herndon, T. A. Cram, C. S. Velden, R. J. Murnane, and J. D. Hawkins, 2007: Estimating hurricane wind structure in the absence of aircraft reconnaissance. *Wea. Forecasting,* **22,** 89–101, doi:10.1175/WAF985.1.

Lawrence, M. B., B. M. Mayfield, L. A. Avila, R. J. Pasch, and E. N. Rappaport, 1998: Atlantic hurricane season of 1995. *Mon. Wea. Rev.,* **126,** 1124–1151, doi:10.1175/1520-0493(1998)126<1124:AHSO>2.0.CO;2.

Mueller, K. J., M. DeMaria, J. A. Knaff, J. P. Kossin, and T. H. Vonder Haar, 2006: Objective estimation of tropical cyclone wind structure from infrared satellite data. *Wea. Forecasting,* **21,** 990–1005, doi:10.1175/WAF955.1.

Olander, T. L., and C. S. Velden, 2007: The advanced Dvorak technique: Continued development of an objective scheme to estimate tropical cyclone intensity using geostationary infrared satellite imagery. *Wea. Forecasting,* **22,** 287–298, doi:10.1175/WAF975.1.

Powell, M. D., and P. G. Black, 1990: The relationship of hurricane reconnaissance flight-level wind measurements to winds measured by NOAA's oceanic platforms. *J. Wind Eng. Ind. Aerodyn.,* **36,** 381–392, doi:10.1016/0167-6105(90)90322-4.

——, E. W. Uhlhorn, and J. D. Kepert, 2009: Estimating maximum surface winds from hurricane reconnaissance measurements. *Wea. Forecasting,* **24,** 868–883, doi:10.1175/2008WAF2007087.1.

Reasor, P. D., R. Rogers, and S. Lorsolo, 2013: Environmental flow impacts on tropical cyclone structure diagnosed from airborne Doppler radar composites. *Mon. Wea. Rev.,* **141,** 2949–2969, doi:10.1175/MWR-D-12-00334.1.

Rogers, R., S. Lorsolo, P. Reasor, J. Gamache, and F. Marks, 2012: Multiscale analysis of tropical cyclone kinematic structure from airborne Doppler radar composites. *Mon. Wea. Rev.,* **140,** 77–99, doi:10.1175/MWR-D-10-05075.1.

Sampson, C. R., and A. J. Schrader, 2000: The Automated Tropical Cyclone Forecasting System (version 3.2). *Bull. Amer. Meteor. Soc.,* **81,** 1231–1240, doi:10.1175/1520-0477(2000)081<1231:TATCFS>2.3.CO;2.

Schwerdt, R. W., F. P. Ho, and R. W. Watkins, 1979: Meteorological criteria for standard project hurricane and probable maximum hurricane wind fields, Gulf and East Coasts of the United States. NOAA Tech. Rep. NWS 23, 317 pp. [Available online at http://www.nws.noaa.gov/oh/hdsc/Technical_reports/TR23.pdf.]

Shea, D. J., 1972: The structure and dynamics of the hurricane's inner core region. Colorado State University Atmos. Sci. Paper 182, 134 pp. [Available online at http://digitool.library.colostate.edu///exlibris/dtl/d3_1/apache_media/L2V4bGlicmlzL2R0bC9kM18xL2FwYWNoZV9tZWRpYS8yNjU3.pdf.]

Ueno, M., and K. Bessho, 2011: A statistical analysis of near-core surface wind asymmetries in typhoons obtained from QuikSCAT data. *J. Meteor. Soc. Japan,* **89,** 225–241, doi:10.2151/jmsj.2011-304.

Uhlhorn, E. W., P. G. Black, J. L. Franklin, M. Goodberlet, J. Carswell, and A. S. Goldstein, 2007: Hurricane surface wind measurements from an operational stepped frequency microwave radiometer. *Mon. Wea. Rev.,* **135,** 3070–3085, doi:10.1175/MWR3454.1.

——, B. W. Klotz, T. Vukicevic, P. D. Reasor, and R. F. Rogers, 2014: Observed hurricane wind speed asymmetries and relationships to motion and environmental shear. *Mon. Wea. Rev.,* **142,** 1290–1311, doi:10.1175/MWR-D-13-00249.1.

Vickery, P. J., F. J. Masters, M. D. Powell, and D. Wadhera, 2009: Hurricane hazard modeling: The past, present, and future. *J. Wind Eng. Ind. Aerodyn.,* **97,** 392–405, doi:10.1016/j.jweia.2009.05.005.

Weatherford, C. L., and W. M. Gray, 1988: Typhoon structure as revealed by aircraft reconnaissance. Part I: Data analysis and climatology. *Mon. Wea. Rev.,* **116,** 1032–1043, doi:10.1175/1520-0493(1988)116<1032:TSARBA>2.0.CO;2.

Willoughby, H. E., R. W. R. Darling, and M. E. Rahn, 2006: Parametric representation of the primary hurricane vortex. Part II: A new family of sectionally continuous profiles. *Mon. Wea. Rev.,* **134,** 1102–1120, doi:10.1175/MWR3106.1.

Wood, V. T., L. W. White, H. E. Willoughby, and D. P. Jorgensen, 2013: A new parametric tropical cyclone tangential wind profile model. *Mon. Wea. Rev.,* **141,** 1884–1909, doi:10.1175/MWR-D-12-00115.1.

Zehr, R. M., and J. A. Knaff, 2007: Atlantic major hurricanes, 1995–2005—Characteristics based on best track, aircraft, and IR images. *J. Climate,* **20,** 5865–5888, doi:10.1175/2007JCLI1652.1.

Zhang, J. A., and E. W. Uhlhorn, 2012: Hurricane sea surface inflow angle and an observation-based parametric model. *Mon. Wea. Rev.,* **140,** 3587–3605, doi:10.1175/MWR-D-11-00339.1.